Gate-tunable Rashba spin-orbit coupling and spin polarization at diluted oxide interfaces

Yulin Gan,* Yu Zhang, Dennis Valbjørn Christensen, Nini Pryds, and Yunzhong Chen†
Department of Energy Conversion and Storage, Technical University of Denmark, Risø Campus, 4000 Roskilde, Denmark

(Received 10 July 2019; published 16 September 2019)

A diluted oxide interface of $LaAl_{1-x}Mn_xO/SrTiO_3$ (LAMO/STO) provides a new way of tuning the ground states of the interface between the two band insulators of LAO and STO from metallic/superconducting to highly insulating. Increasing the Mn doping level (x) leads to a delicate control of the carrier density as well as a raise in the electron mobility and spin polarization. Herein, we demonstrate a tunable Rashba spin-orbit coupling (SOC) and spin polarization of LAMO/STO ($0.2 \leqslant x \leqslant 0.3$) by applying a back gate. The presence of SOC causes splitting of the energy band into two branches by a spin splitting energy. The maximum spin splitting energy depends on the Mn doping and decreases with the increasing Mn content and then vanishes at $x = 0.3$. The carrier density dependence of the spin splitting energy for different compositions shows a dome-shaped behavior with a maximum at different normalized carrier densities. These findings have not yet been observed in LAO/STO interfaces. A fully back-gate-tunable spin-polarized two-dimensional electron liquid is observed at the interface with $x = 0.3$ where only d_{xy} orbits are populated ($5.3 \times 10^{12}\,\mathrm{cm}^{-2} \leqslant n_s \leqslant 1.0 \times 10^{13}\,\mathrm{cm}^{-2}$). The present results shed light on unexplored territory in SOC at STO-based oxide heterostructures and make LAMO/STO an intriguing platform for spin-related phenomena in $3d$ electron systems.

DOI: 10.1103/PhysRevB.100.125134

I. INTRODUCTION

The two-dimensional electron liquid (2DEL) at the interface or surface of $SrTiO_3$ (STO) has attracted extensive attention due to its extraordinary physical properties such as spin-orbit coupling [1–4], ferromagnetism [5–7], superconductivity [8–10], and quantum Hall effect [11]. These properties can also be controlled through manipulation of the carrier concentration using electric fields or chemical doping. So far, the archetypical system remains the 2DEL formed at the interface between two band insulators of $LaAlO_3$ (LAO) and STO. Due to the large permittivity of the STO substrate at low temperature [12], the transport properties of the 2DELs, such as carrier density and mobility, can be modulated significantly by electrostatic gating [13,14]. Gate-tunable metal-insulator transitions [15,16], superconductivity [8], Rashba spin-orbit coupling [1], and spin polarization [17] have been reported, which could pave the way for developing future novel electronic/spin-electronic devices [18,19].

Based on the chemical doping and a manganite-buffer-layer–induced modulation doping [20,21], a new modulation doping made by alloying $LaMnO_3$ (LMO) with LAO not only suppresses the sheet carrier density (n_s) gradually by increasing the Mn doping level ($0 \leqslant x \leqslant 1$) but also leads to the realization of spin-polarized 2DELs at $x = 0.3$ [22]. This magnetically diluted oxide interface reveals the evolution of the electronic state at STO-based interfaces as a function of carrier density and provides new and unexplored electronic states other than the intensively investigated bare LAO/STO interface [8,23]. Four kinds of electronic ground states have been created at diluted interfaces by controlling the Mn doping level: (i) For $0 \leqslant x \leqslant 0.2$, conductivity occurs in two bands; (ii) for $0.225 \leqslant x \leqslant 0.275$, only a single band is occupied; (iii) for $x = 0.3$, the single band occupancy remains; however, the 2DEL becomes spin polarization; and (iv) for $0.3 < x \leqslant 1$, an insulating state is observed. This provides a convenient handle to investigate the gate-tunable transport properties of different as-grown ground states.

Generally, the 2DEL of STO-based interfaces is confined in an asymmetric quantum well located on the STO side. The absence of spatial inversion symmetry at the heterointerfaces leads to a strong Rashba spin-orbit coupling (SOC) [1]. In two-dimensional (2D) electron systems, weak localization (WL) and weak antilocalization (WAL) are two quantum interference effects resulting from electron phase coherence and spin-orbit coupling. These quantum interference effects are related to the three scattering processes—inelastic scattering, spin-orbit scattering, and elastic scattering [24]. Previous studies have shown that the SOC strength can be modulated by a top and/or back gate [1,3,4,23,25]. Analyzing the WAL/WL, some groups reported that the strength of the SOC decreases monotonously upon decreasing the back-gate voltages [1,10] or even show a maximum at the d_{xy}-d_{xz}/d_{yz} crossing region at the LAO/STO interface [3]. Previous studies of the SOC at STO-based conducting interfaces implemented the weak SOC approximation [26], which assumes that the elastic scattering characteristic field is much stronger than the SOC scattering characteristic field. A significant mobility (μ) enhancement at the $LaAl_{1-x}Mn_xO/SrTiO_3$ (LAMO/STO) interfaces is observed when increasing the Mn doping and leads to a decrease of the elastic scattering field. When the elastic scattering field is so weak that it is comparable with the SOC scattering field, the weak SOC approximation is not applicable anymore, and it remains to be investigated what happens to the

*Corresponding author: yuga@dtu.dk
†Corresponding author: yunc@dtu.dk

spin-orbit effect here. Our LAMO/STO system exhibits different ground states with the possibility to enhance the mobility by increasing the Mn doping level. The LAMO/STO system, therefore, provides an interesting platform to investigate the gate-tunable SOC where the weak SOC approximation is not applicable.

Moreover, the anomalous Hall effect (AHE) observed in the LAMO/STO interface with $x = 0.3$ implies the existence of a spin-polarized state with a single band of d_{xy} electrons. In a previous report, Stornaiuolo *et al.* [17,27] has shown an electric-field-tunable spin-polarized and superconducting 2DEL at the ferromagnetic $EuTiO_3$ buffered LAO/STO interface with higher carrier density where both the d_{xy} and d_{xz}/d_{yz} bands are populated. The AHE observed in the current work is a result of spin-polarized d_{xy} electrons, making our system interesting for investigation of the gate-controlled magnetism or spin polarization.

In this paper, we systematically investigated the back-gate-tunable transport properties of various electronic ground states at LAMO/STO heterostructures for different Mn doping ($0.2 \leqslant x \leqslant 0.3$). We observed a gate-tunable SOC in the heterointerfaces with $x = 0.2$, 0.225, and 0.25 and gate-tunable spin-polarized d_{xy} electrons for $x = 0.3$. For $x = 0.2$, the weak SOC approximation is available, and 2DEL exhibits a dome-shaped dependence of spin splitting energy on carrier density, with the maximum occurring at the Lifshitz transition point. However, this approximation cannot be applied to analyze the WAL for the $x = 0.225$ and 0.25, since the elastic scattering is comparable with the SOC scattering. In addition, the strongest spin splitting energy of different samples decreases with the increasing Mn doping level. On the other side, the spin polarization of d_{xy} electrons is fully tunable by the electric field effect at $x = 0.3$ with $5.3 \times 10^{12}\,\mathrm{cm}^{-2} \leqslant n_s \leqslant 1.0 \times 10^{13}\,\mathrm{cm}^{-2}$.

II. EXPERIMENTAL METHOD

The $LaAl_{1-x}Mn_xO_3$ thin films, with $x = 0.2$, 0.225, 0.25, and 0.3, were grown by pulsed laser deposition (PLD) using a KrF laser on TiO_2-terminated $5 \times 5 \times 0.5$ mm (001) STO substrates. Before the deposition, a hard mask made from amorphous $LaMnO_3$ (LMO) was patterned on the STO substrates in a Hall bar geometry by optical lithography ($W = 50\,\mu$m, $L = 500\,\mu$m) [28]. The film thickness was kept constant at eight unit cells, and the film growth of the unpatterned sample was realized in a layer-by-layer 2D growth mode as described in Ref. [22]. A pulsed laser with a wavelength of 248 nm, a repetition frequency of 1 Hz, and laser fluence of $4.0\,\mathrm{J/cm}^2$ was used to ablate the LAMO ceramic targets. Films were deposited at 650 °C, in $1 - 3 \times 10^{-5}$ mbar of O_2 and a constant distance between target and substrate of $\sim$ 50 mm. After the growth of the film, the samples were cooled under the deposition pressure at a rate of 15 °C/min to room temperature.

The electrical contacts to the interface of the Hall bar samples were made using ultrasonically wire-bonded aluminum wires as electrodes. A uniform thin layer of silver paint is applied on the back of the substrate as the back-gate electrode. A cryogenic cryogen-free measurement system was employed to characterize the magnetotransport at 2 K with various back-gate voltages (V_{bg}) and perpendicular magnetic field up to 15 T. The V_{bg} is initially ramped to the highest positive value (80 V for $x = 0.2$, 0.225, and 0.3; 40 V for $x = 0.25$) and is then swept in the negative direction with steps of 10 V while measuring the V_{bg}-dependent transport characteristics until the metal-insulator transitions occur. The V_{bg}-dependent sheet resistances of all samples are shown in Fig. S1 (see Supplemental Material [29]). In all cases, the leakage current was less than 1 nA and the LMO hard masks are totally insulating.

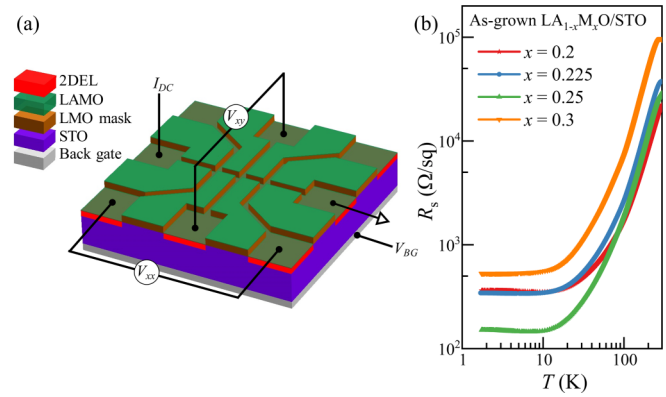

FIG. 1. (a) Sketch of the $LaAl_{1-x}Mn_xO_3/SrTiO_3$ devices under the various back-gate voltages. (b) Temperature dependence of the sheet resistance (R_s) for as-grown states with different Mn doping concentrations (x).

III. RESULTS AND DISCUSSION

Figure 1(a) displays a sketch of the back-gated LAMO/STO interface patterned in the Hall bar geometry. A back-gate bias V_{bg} is applied across the insulating STO substrate. Based on the phase diagram obtained in Ref. [22], we have chosen four representative compositions of $x = 0.2$, 0.225, 0.25, and 0.3 in order to investigate the effect of back-gate field on the interfacial conductivity of various ground states. The corresponding as-grown properties at 2 K are listed in Table I, and the temperature-dependent sheet resistances are shown in Fig. 1(b). All interfaces show typical metallic behavior. For $x = 0.2$, the electrons are populated in both the d_{xy} and the d_{xz}/d_{yz} bands, showing a typical two-band behavior. When $0.225 \leqslant x \leqslant 0.3$, only d_{xy} electrons contribute to the interfacial conduction because the electrons in the d_{xz}/d_{yz} bands are depleted. Moreover, at $x = 0.3$, the interfacial 2DEL becomes spin-polarized due to the proximity effect from ferromagnetic LAMO layer.

The Hall resistance (R_{xy}) measurements at different back-gate voltages reveal an effective modulation of the carrier density. The back-gate–controlled Hall effect can be divided into the three regimes described below: (i) for $0.2 \leqslant x \leqslant 0.225$ under all V_{bg} investigated and $x = 0.25$ at $-10\,\mathrm{V} \leqslant V_{bg} \leqslant 10\,\mathrm{V}$, the Hall effect is suggestive of an ordinary Hall effect (OHE) with one or two kinds of carriers, as shown in Figs. 2(a)–2(c); (ii) for $x = 0.25$ at $20\,\mathrm{V} \leqslant V_{bg} \leqslant 40\,\mathrm{V}$, the Hall resistance curves show the feature of two-carrier transport with AHE, which are discussed in detail in the Supplemental Material [29] (see Fig. S6); (iii) for $x = 0.3$ shown in Fig. 3(a), the Hall resistance shows a typical behavior of

TABLE I. Transport properties for different as-grown states of $LaAl_{1-x}Mn_xO_3/SrTiO_3$ interfaces.

Mn component (x)	n_{tot} (cm^{-2})	μ_{tot} (cm^2/Vs)	Conduction band	Magnetism
0.2	3.90×10^{13}	568	$d_{xy} + d_{xz}/d_{yz}$	×
0.225	2.54×10^{13}	597	d_{xy}	×
0.25	2.14×10^{13}	1566	d_{xy}	×
0.3	0.74×10^{13}	1613	d_{xy}	√

AHE with only one type of carrier. The Hall effect is linear at lower back-gate biases, whereas above a critical voltage (V_c) the Hall effect becomes nonlinear with an anticlockwise bending of the curve at high field. For $0.2 \leqslant x \leqslant 0.225$ under all V_{bg} investigated and $x = 0.25$ at $-10\,V \leqslant V_{bg} \leqslant 10\,V$, the linear and nonlinear Hall curves originate from the OHE with one-carrier and two-carrier transports, respectively, analogous to the Hall effect reported in previous works [9,22]. Such a transition from a linear to a nonlinear behavior is interpreted as evidence of a Lifshitz transition as the carrier occupation changes from only the d_{xy} bands to both the d_{xy} and d_{xz}/d_{yz} bands. Previous theoretic [30] and experimental reports [9] suggest that the tetragonal distortion and quantum confinement along z direction push the in-plane d_{xy} bands down in energy compared to the out-of-plane $d_{xz/yz}$ bands. Therefore, when the Fermi surface enters the bottom of the $d_{xz/yz}$ bands, both the d_{xy} and $d_{xz/yz}$ bands become populated. Following the two-band conduction model in Refs. [9] and [31], we extract the electron densities n_{LF} and n_{HF} from the Hall coefficients ($R_h = dR_{xy}/dB$) near 0 and 15 T, which reflect, approximately, the carrier density in the high-mobility band $n_{LF} = 1/[eR_h(B \to 0)]$ and the total carrier density $n_{HF} = 1/[eR_h(B \to \infty)]$, respectively. Because the presence of AHE in $x = 0.25$ at $20\,V \leqslant V_{bg} \leqslant 40\,V$ leads to a correction to Hall resistance at low field, the n_{LF} are extracted after removing the correction from AHE (Fig. S6, Supplemental Material [29]).

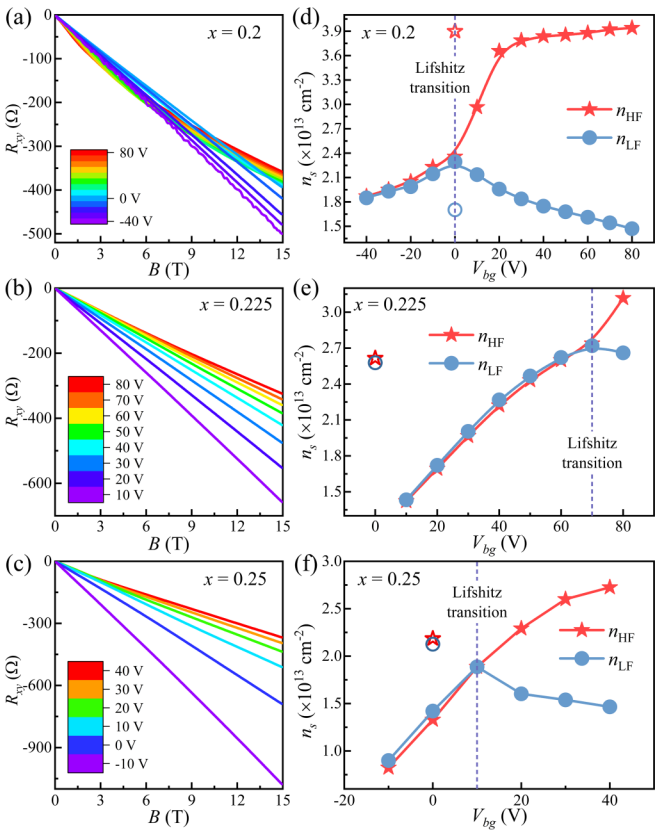

FIG. 2. Hall resistance and carrier density as a function of the gate voltage at interfaces with $x = 0.2$, 0.225, and 0.25. (a)–(c) The B-dependent Hall resistance for various gate voltages for $LaAl_{1-x}Mn_xO_3/SrTiO_3$ heterointerfaces with $x = 0.2$, 0.225, and 0.25, respectively. (d)–(f) The n_{LF} and n_{HF} extracted from low field (0 T) and high field (15 T) of R_{xy}-B curves as a function of gate voltage for different Mn doping levels. The open scatter plots show the as-grown carrier density for each state.

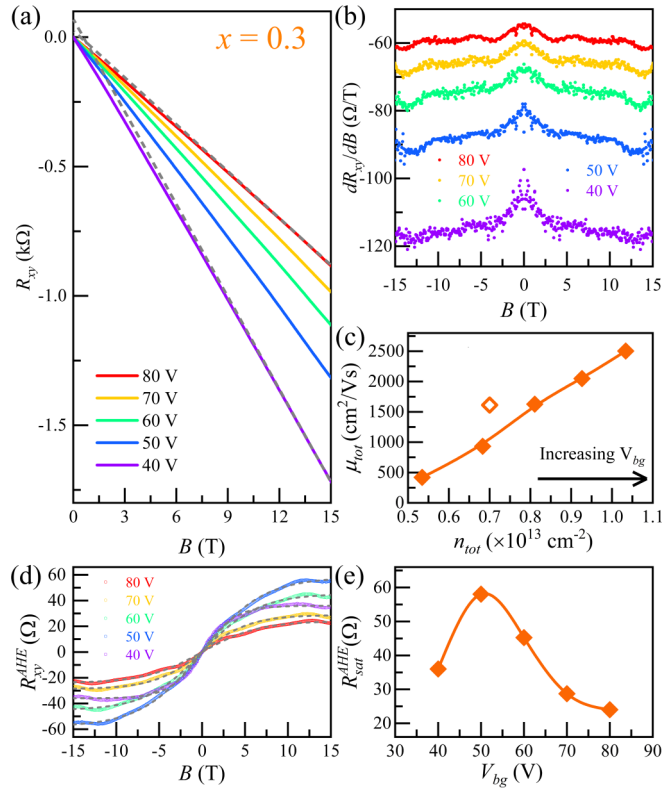

FIG. 3. Gate-tunable anomalous Hall effect (AHE), carrier density, and mobility at spin-polarized interface with $x = 0.3$. (a) The nonlinear R_{xy} vs B from 40 to 80 V. (b) The corresponding evolution of Hall coefficient $R_h = dR_{xy}/dB$. (c) The carrier density and mobility extracted from the fitting ordinary Hall resistance. The open rhombus shows the as-grown carrier density and mobility for $x = 0.3$. (d) Magnetic-field-dependent R_{xy}^{AHE} under different V_{bg}. The dashed line is the fitting data of anomalous Hall resistance. (e) The saturated Hall resistance R_{sat}^{AHE} as a function of V_{bg}.

A gate-induced Lifshitz transition is clearly demonstrated in the V_{bg}-dependent carrier density as shown in Figs. 2(d)–2(f). The n_{LF} and n_{HF} are approximately identical at lower back-gate voltages, which is in agreement with a linear Hall resistance where only the d_{xy} orbits are populated. Above the critical voltage (V_c), n_{LF} shows a clear deviation from n_{HF}, which is the typical character of nonlinear Hall resistance expected from electron transport in both d_{xy} and d_{xz}/d_{yz} bands. The critical values of V_c for $x = 0.2$, 0.225, and 0.25 are 0, 70, and 10 V, respectively. The corresponding Lifshitz density (n_c) is $2.3 \times 10^{13}\,\mathrm{cm}^{-2}$, $2.7 \times 10^{13}\,\mathrm{cm}^{-2}$, and $1.9 \times 10^{13}\,\mathrm{cm}^{-2}$, respectively, which are similar to the reported value of $n_c \approx 1.7{-}3.1 \times 10^{13}\,\mathrm{cm}^{-2}$ [3,9,22]. The minor differences in the critical carrier density among different samples might be due to the gate-dependent effective band structure [23].

Furthermore, for the interface with $x = 0.3$ hosting the spin-polarized 2DEL, the Hall resistance traces at different V_{bg} shown in Fig. 3(a) are nonlinear with a clockwise bend at low fields, which are different from those of the two-band conduction but similar to AHE with one-carrier transport reported in Ref. [22]. Here, the evolutions of Hall coefficients R_h as a function of B in Fig. 3(b) further suggest that the B-dependent Hall resistances are nonlinear at low magnetic field and become linear at higher magnetic field, forming a peak around $B = 0$. Such nonlinear behavior of R_{xy} cannot be modeled by the typical two-band model but rather by AHE with only d_{xy} electrons. Therefore, such nonlinear Hall resistance is a sum of two contributions: the linear contribution from the OHE with one-carrier transport and a nonlinear contribution from the AHE. The anomalous Hall resistance (R_{xy}^{AHE}) can be described using the Langevin-type function [32]. The total Hall resistance can then be expressed as $R_{xy} = R_{xy}^{\mathrm{OHE}} + R_{xy}^{\mathrm{AHE}} = -B/(en) + R_{\mathrm{sat}}^{\mathrm{AHE}} \tanh(B/B_c)$. Here, B_c is the critical field above which R_{xy}^{AHE} saturates to the value of $R_{\mathrm{sat}}^{\mathrm{AHE}}$. The $R_{\mathrm{sat}}^{\mathrm{AHE}}$ is proportional to the saturation magnetization.

The fit of the AHE curve successfully extracts the ordinary Hall resistance (R_{xy}^{OHE}) and anomalous Hall resistance (R_{xy}^{AHE}). From the ordinary Hall resistance, the carrier density for different V_{bg} is extracted and is used to calculate the mobility. As shown in Fig. 3(c), with the increase of V_{bg}, the carrier density is changed from $5.3 \times 10^{12}\,\mathrm{cm}^{-2}$ at 40 V to $1.0 \times 10^{13}\,\mathrm{cm}^{-2}$ at 80 V, and the mobility increases by almost 6 times from 420 to 2503 $\mathrm{cm}^2/\mathrm{Vs}$. It is worth noting that the carrier density of all samples could not return to their as-grown states after removing the gate voltage, which is common behavior in oxide interface systems [8,25]. This leads to a sharp V_{bg}-induced metal-insulator transition under 40 V at $x = 0.3$. The as-grown data are shown in Figs. 2(d)–2(f) and 3(c) as open symbols, whereas the results after cycling the back gate are shown as filled symbols. A possible reason for this behavior is that with the application of positive gate bias, some electrons are trapped in defects at the in-gap states [33]. On the other side, the B-dependent anomalous Hall resistances at various V_{bg} shown in Fig. 3(d) are extracted by deducting the ordinary Hall resistance from total Hall resistance. As summarized in Fig. 3(e), the value of $R_{\mathrm{sat}}^{\mathrm{AHE}}$ increases from 24.0 to 58.1 Ω as V_{bg} decreases from 80 to 50 V, and it finally decreases to 36.0 Ω at $V_{bg} = 40$ V. Our results suggest that the spin polarization

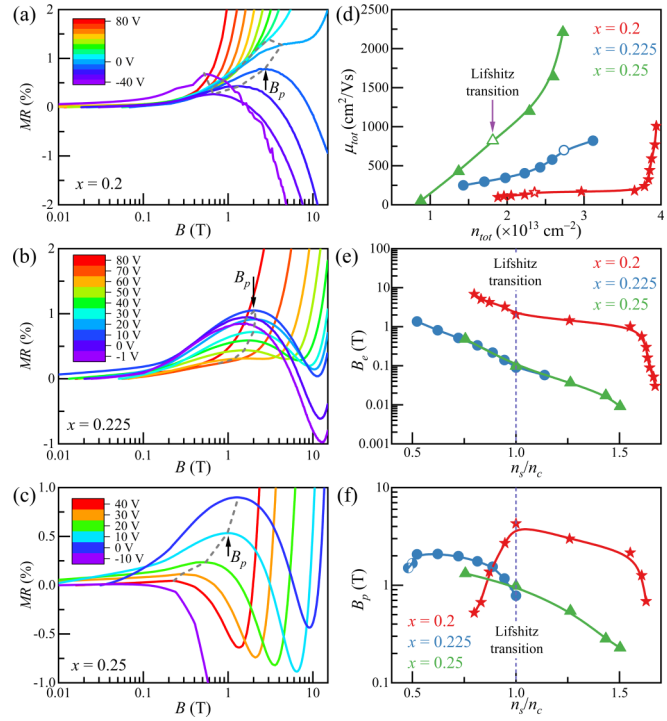

FIG. 4. Analysis of the magnetoresistance data at interfaces with $x = 0.2$, 0.225, and 0.25. (a)–(c) The field-dependent magnetoresistance measurements carried out under different back-gate voltages for $x = 0.2$, 0.225, and 0.25, respectively. The gray dash lines mark the position of B_p. In order to highlight the anomalous magnetoresistance at the low magnetic field, the MR curves are shown in a semilogarithmic plot of B. (d) The evolutions of mobility as a function of carrier density. The open star, circle, and triangle are the corresponding Lifshitz transitions for $x = 0.2$, 0.225, and 0.25, respectively. (e) The evolutions of elastic scattering fields reduced by n_{tot} and μ_{tot} as the function of carrier density normalized by the Lifshitz density (n_c). (f) The evolutions of B_p extracted from (a–c) as the function of carrier density normalized by the Lifshitz density (n_c). The left and right half-filled circles mark the interfaces with $x = 0.225$ at −1 and 0 V, where the Hall resistance is undetectable and their normalized carrier density is lower than 0.5.

of d_{xy} electrons in our system is fully gate tunable. And the decrease of the $R_{\mathrm{sat}}^{\mathrm{AHE}}$ at $V_{bg} = 40$ V might indicate the presence of the Kondo effect [34].

We now turn to the gate modulation of the longitudinal resistance. The magnetoresistance [MR: $\Delta R_{xx} = R_{xx}(B)/R_{xx}(0) - 1$] of $x = 0.2$, 0.225, and 0.25 under different electric fields is shown in Figs. 4(a)–4(c) as a function of B. At back-gate voltages higher than 40 V for $x = 0.2$ and 70 V for $x = 0.225$, the MR is positive and quadratic at all measured magnetic fields, which is a typical behavior of ordinary MR primarily caused by the classical Lorentz force. When V_{bg} is below these values, a sharp increase of MR starts to appear at the low field and then drops after reaching a peak with increasing field. This phenomenon is a typical behavior of WAL, where the SOC counteracts the WL to form a peak superimposed on the negative magnetoresistance background caused by WL. For $x = 0.25$ at −10 V, only a negative MR is detected up to the largest accessible magnetic field (15 T), which is the typical signature of WL, resulting in a

V_{bg}-induced WAL-WL transition. Therefore, every MR curve can be considered as a superposition of three components in different proportions, i.e., a sharp increase of MR around the zero field, negative MR and the quadratic and positive MR, which come from the WAL, WL and classical MR from Lorentz force, respectively.

The WAL/WL is a manifestation of the quantum interference behaviors of electrons, which is normally determined by inelastic (phase breaking) scattering, elastic scattering, and SOC scattering. In order to further analyze the quantum correction of WAL/WL to the MR, three characteristic magnetic fields $[B_k = \hbar/(4eD\tau_k), k = i, e, so]$ are introduced to characterize B-dependent quantum correction based on three scattering processes. Here, τ_i, τ_e, and τ_{so} are the inelastic scattering time, the elastic scattering time, and the spin-orbit scattering time, respectively. The $D = v_F^2\tau_e/2$ is the diffusion constant given by the Drude model. The elastic scattering time τ_e describes the characteristic time of an electron in an available closed path for electron backscattering. The inelastic scattering time τ_i is the characteristic time for the electron to avoid inelastic phase breaking [35]. When the elastic scattering time (τ_e) of electrons is much less than the inelastic scattering time (τ_i), i.e., $\tau_e \ll \tau_i$ and $B_e \gg B_i$, in absence of a significant SOC, the interference of backscattered electron waves is constructive, leading to the weak localization, such as observed at the interface with $x = 0.25$ at -10 V in Fig. 4(c). In the WL, the electrons are at localized states. Conversely, if $\tau_e > \tau_i$ (i.e., $B_e < B_i$), the elastic scattering time is so long that the electrons no longer return to their origin to cause a constructive interference, where the electrons are at extended states. For the extended states, the MR is mainly caused by the Lorentz force, such as observed in the interfaces with $x = 0.2$ at 50–80 V and $x = 0.225$ at 80 V, as shown in Figs. 4(a) and 4(b). This means that the WL takes place in fields $B_e \gg B_i$ (i.e., $\tau_e \ll \tau_i$), namely, in the diffusive regime. On the other hand, the spin-orbit scattering time τ_{so} describes the spin phase shift on the order of π caused by the effective magnetic field of the SOC [35]. When the SOC appears in the diffusive regime with $B_e > B_{so} > B_i$, the spin of carriers would add an extra phase factor that destroys the constructive interference, leading to the destructive interference to counteract the WL—this is the character of WAL. Here, the B_e could be rewritten as $B_e = e/(2hn_s\mu^2)$, which contains only the carrier density and the mobility. As shown in Fig. 4(d), the effective mobility ($\mu_{tot} = 1/[en_{tot}R_{xx}(0)]$) decreases when the carrier density (n_{tot}) is reduced, which is the same with the case of $x = 0.3$ shown in Fig. 3(c). Notably, the samples with higher Mn always show higher mobility for the same carrier density. The deduced B_e are shown in Fig. 4(e) as a function of sheet carrier density normalized by the Lifshitz density, (n_s/n_c). Here, the adoption of normalized carrier density (n_s/n_c) effectively distinguishes the contributions of the one-band region or two-band region. The $0 < n_s/n_c < 1$, $n_s/n_c = 1$, and $n_s/n_c > 1$ represent the one-band region, Lifshitz transition point, and two-band region, respectively. For all samples, the back-gate–controlled B_e decreases monotonically with increasing normalized carrier density due to the monotonically increasing mobility and sheet carrier density.

In the magnetoresistance measurements of the WAL/WL, the applied magnetic field (B) could break the time-reversal symmetry and diminish the interference of the time-reversed paths, leading to the compensation of the SOC and WL. As shown in Figs. 4(a)–4(c), for lower $B(B_i < B < B_{so} < B_e)$ the MR raises sharply with an increase of B, where the SOC reduces the net interference contribution from WL to form WAL. With the further increase of B, the MR reaches a maximum at B_p after which the spin-orbit coupling cannot contribute to the quantum interference, marking the B-induced WAL-WL transition [36]. With a further increase of B, when $B_i < B_{so} < B < B_e$, the MR continues to decrease due to the suppression of WL. Finally, when the B is so high, i.e., $B_i < B_{so} < B_e < B$, quantum interferences are negligible and only the classical positive MR from Lorentz force is detectable. Therefore, the magnetic field B_p signifies the critical field for the B-induced WAL-WL transition, which roughly reflects the SOC strength [3,37]. The critical fields (B_p) are extracted directly from the clear peaks in WAL curves. However, for $x = 0.2$ at 0−40 V and $x = 0.225$ at 70 V, there is no observed peak because the weak WAL is overlapped with the classic MR. The corresponding B_p is extracted after removing the classic MR fitted by the two-band model in Ref. [22] (Fig. S2, Supplemental Material [29]). As shown in Fig. 4(f), the values of B_p change between 0.5−4.3 T, 0.8−2.1 T, and 0.2−1.3 T for $x = 0.2$, 0.225, and 0.25, respectively, which are comparable to the observations in earlier work where the critical fields were found to be 0.3–4.0 T [3]. For $x = 0.2$, with the accumulation of the carriers, the B_p first reaches a maximum value at the Lifshitz point and then decreases. This is similar to the nonmonotonically tunable spin-orbit coupling in STO-based heterointerfaces reported in Ref. [3]. Here, this strongest SOC observed at the Lifshitz transition is interpreted as an enhanced SOC due to the orbit hybridization at the d_{xy}-d_{xz}/d_{yz} crossing region. However, for $x = 0.225$ and 0.25, as the carriers are reduced, the values of B_p increase to a maximum and then decrease sharply or disappear just before a sharp metal-insulator transition occurs. Interestingly, the maximum values of B_p appear at $n_s/n_c = 0.52$ for $x = 0.225$ and at $n_s/n_c = 0.76$ for $x = 0.25$, where the Fermi-level is located in the deeper d_{xy} band. Besides, no enhanced SOC occurs at the Lifshitz transition points. These phenomena at $x = 0.225$ and 0.25 are different from the observation at $x = 0.2$. The observed maximum B_p for different doping levels decreases from 4.3 to 1.3 T with the increase of Mn content from 0.2 to 0.25.

The shape of B_p presented above reveals qualitatively the evolutions of SOC as a function of carrier density. As the consequence of SOC, the electron energy state at the Fermi surface splits into two branches characterized by a spin splitting energy. In order to analyze the characteristic field of SOC and the spin splitting energy in more detail, the fit of the magnetoconductance (MC) is carried out to estimate the contributions from the WL, SOC, and classical MC from Lorentz force. The MC $[\Delta\sigma_{xx} = \sigma_{xx}(B) - \sigma_{xx}(0)]$ normalized by a universal value of conductance ($G_0 = e^2/\pi h \approx 1.2 \times 10^{-5}$ S) is shown in Figs. S4(a)–S4(c) as a function of B for various V_{bg}. Because of the larger quadratic field dependence of MC, for weak SOC in MR, the WAL in $\sigma_{xx}(B)$ is too weak to extract the SOC in samples with $x = 0.2$ at $30\text{ V} \leqslant V_{bg} \leqslant 40\text{ V}$, $x = 0.225$ at $V_{bg} = 70$ V, and $x = 0.25$ at $20\text{ V} \leqslant V_{bg} \leqslant 40$ V (Fig. S3, Supplemental Material [29]).

Therefore, the significant SOC mainly emerges for $x = 0.2$ at $-40\,\mathrm{V} \leqslant V_{\mathrm{bg}} \leqslant 20\,\mathrm{V}(0.8 \leqslant n_s/n_c \leqslant 1.6)$, for $x = 0.225$ at $10\,\mathrm{V} \leqslant V_{\mathrm{bg}} \leqslant 60\,\mathrm{V}(0.5 \leqslant n_s/n_c \leqslant 0.9)$, and for $x = 0.25$ at $0\,\mathrm{V} \leqslant V_{\mathrm{bg}} \leqslant 10\,\mathrm{V}(0.8 \leqslant n_s/n_c \leqslant 1.0)$. Previous studies [1,2] show that the WAL at conductive STO-based interfaces is well described by two theoretical models developed by Hikami, Larkin, and Nagaoka (HLN) [38,39] and Iordanskii, Lyanda-Geller, and Pikus (ILP), respectively [40]. However, these models are valid only for a weak SOC in the diffusive regime, where the WL/WAL takes place at $B \ll B_e$ and $B_{so} \ll B_e$ for which the B_e does not appear explicitly [41]. These methods give good fits for all WAL/WL curves, but the shape of the fitting parameter B_{so} is in accordance with the prediction from B_p only for $x = 0.2$ (more detailed discussions in Supplemental Material [29], Sec. 3). Because the extracted B_{so} exceeds B_e for $x = 0.225$ at $40\,\mathrm{V} \leqslant V_{\mathrm{bg}} \leqslant 60\,\mathrm{V}$ and for $x = 0.25$ at 10 V as seen in Figs. S4(e) and S4(f), the two methods are not available for $x = 0.225$ and 0.25, which indicates the failure of the weak SOC approximation. In this scenario, the strong SOC observed at the interfaces with higher mobility leads to the fact that B_e is comparable with the B_{so}, so the weak SOC approximation fails to describe the SOC in WAL at $x = 0.225$ and 0.25.

Here, the Maekawa-Fukuyama (MF) theory [26] is applied for the case of strong SOC to analyze the WAL/WL. Considering a pronounced contribution from Lorentz force to MC in the entire magnetic field regime, the classical MC gives rise to a parabolic behavior [10,42]. Combining the first-order quantum correction of WL/WAL and the classical MC, the correction to the MC with a negligible Zeeman effect can be expressed as

$$\frac{\Delta\sigma_{xx}(B)}{G_0} = -F\left(\frac{B}{B_1}\right) + F\left(\frac{B}{B_2}\right) + \frac{1}{2}F\left(\frac{B}{B_3}\right) - \frac{1}{2}F\left(\frac{B}{B_4}\right) - A_k\frac{\sigma_{xx}(0)}{G_0}\frac{B^2}{1+CB^2},$$

$$B_1 = B_e + B_{so},$$

$$B_2 = B_i + (B_e + B_{so})\frac{B_{so}}{B_e},$$

$$B_3 = B_i + (B_e + B_{so})\left(\frac{2B_{so}}{B_e - B_{so}}\right),$$

$$B_4 = B_i.$$

Here, the function F is defined as $F(x) = \ln(x) + \psi(1/2 + 1/x)$, where $\psi(x)$ is the digamma function. The parameters A_k and C from the last term describe the classical MC. Using the B_e deduced from the carrier density and mobility, the B_{so} and B_i are obtained directly from the best fits of the experimental data (Fig. S4, Supplemental Material [29]). The shapes of B_{so} for all samples are in accordance with the prediction from B_p in Fig. 4(f), indicating that the MF model successfully captures our observation of the WAL/WL. The SOC characteristic fields are tuned between 0.19–1.14 T, 0.09–0.31 T, and 0.10–0.16 T for $x = 0.2$, 0.225, and 0.25, respectively. Since the SOC contribution mainly stems from d_{xy} electrons, we can derive the relaxation times τ_e, τ_{so}, and τ_i by assuming an average effective mass $m^* = m_e$ [11,43,44].

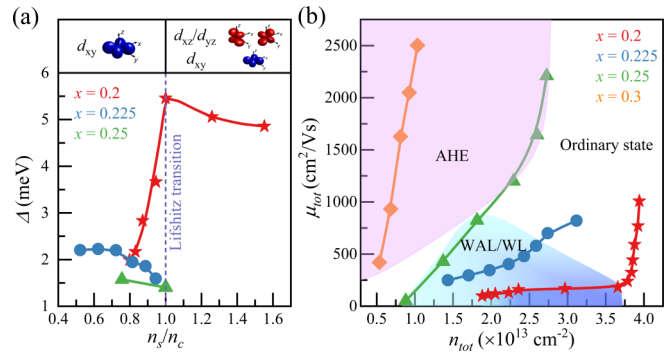

FIG. 5. (a) The spin splitting energy as functions of the sheet carrier density (n_s) normalized by the Lifshitz density (n_c) for the $LaAl_{1-x}Mn_xO_3/SrTiO_3$ interfaces with $x = 0.2$, 0.225, and 0.25. (b) Carrier mobility as a function of carrier density for the four samples. The regions for anomalous Hall effect and robust weak (anti)localization are summarized.

According to the expression in Ref. [1], the spin splitting energy $\Delta = \hbar/\sqrt{\tau_e\tau_{so}}$ is determined by the elastic scattering time and SOC scattering time, and its evolutions are summarized in Fig. 5(a) as a function of normalized carrier density. The interface with $x = 0.2$ has a domelike dependence of Δ on the carrier density, with the peak of 5.5 meV at the Lifshitz point ($n_s/n_c = 1$). The significant local orbital angular momentum induced by the orbital hybridization at the d_{xy}-d_{xz}/d_{yz} crossing area could enhance the SOC and form a dome [3,45]. Here, for a one-carrier region ($0 < n_s/n_c \leqslant 1$), the Δ decreases monotonically with decreasing carrier density, similar to what is observed in previous works [3,10]. In contrast, the spin splitting energies of $x = 0.225$ and 0.25 increase monotonically with the decreasing carrier density, reaching maximum values of 2.2 meV for $x = 0.225$ at $n_s/n_c = 0.52$ and 1.6 meV for $x = 0.25$ at $n_s/n_c = 0.76$, respectively. This was not discussed for the STO-based oxide interfaces so far. A possible explanation for our observations is that for $x = 0.225$ and 0.25, the higher mobility causes a lower B_e, which is comparable with the B_{so}, so the weak SOC approximation ($B_{so} \ll B_e$) will fail to describe such SOC in WAL. At the same time, with the increasing carrier density, the decreasing B_e reduces the probability of electron backscattering. Because the WAL originates from the SOC of the backscattered electrons, the reduction of backscattered electrons further causes the suppression of spin-orbit coupled electrons, when the elastic scattering is comparable with the SOC scattering. For the weak SOC approximation, the influence of B_e on B_{so} is very weak and could be ignored, as in the case of $x = 0.2$ (Fig. S4, Supplemental Material [29]). However, the failure of such approximation at $x = 0.225$ and 0.25 implies a significant influence of B_e on B_{so}. This could also explain the decrease of maximum spin splitting energy from 5.5 to 1.6 meV with the increasing Mn doping from 0.2 to 0.25. Moreover, for $x = 0.3$ [Fig. S5(a)], only classical positive MR is observed at different bias voltages before becoming an insulator, indicating that B_e is lower than B_i and the WAL/WL does not appear.

The gate-tunable transport properties of different electronic states at the diluted oxide interfaces with $0.2 \leqslant x \leqslant 0.3$ are

summarized in Fig. 5(b). Here, we observe the WAL/WL at $0.88 \times 10^{13}\,\mathrm{cm}^{-2} \leqslant n_s \leqslant 3.66 \times 10^{13}\,\mathrm{cm}^{-2}$ in the low-mobility region. With the increase of mobility, the anomalous magnetoresistance caused by WAL/WL changes to classical MR, implying the transition of transport from localized states to extended states.

IV. CONCLUSIONS

In conclusion, we have systematically investigated the electrostatic modulation of the transport properties of LAMO/STO heterointerfaces. Regardless of the carrier density, at the interfaces with lower mobility, where the B_e is high enough and the weak SOC approximation is available, the influence of B_e on B_{so} is negligible. However, for higher mobility samples, where B_e is comparable with B_{so}, a significant suppression of spin splitting energy occurs. Our observations not only mapped the evolution of spin-orbit coupling as a function of carrier density, when the interfaces change from extended state to WAL and then to WL, but also realized the gate-tunable spin polarization of 2DELs. These results make the LAMO/STO system an intriguing platform for future oxide spintronics.

[1] A. D. Caviglia, M. Gabay, S. Gariglio, N. Reyren, C. Cancellieri, and J. M. Triscone, Phys. Rev. Lett. **104**, 126803 (2010).

[2] H. Nakamura, T. Koga, and T. Kimura, Phys. Rev. Lett. **108**, 206601 (2012).

[3] H. Liang, L. Cheng, L. Wei, Z. Luo, G. Yu, C. Zeng, and Z. Zhang, Phys. Rev. B **92**, 075309 (2015).

[4] W. Niu, Y. Zhang, Y. L. Gan, D. V. Christensen, M. V. Soosten, E. J. Garcia-Suarez, A. Riisager, X. Wang, Y. Xu, R. Zhang, N. Pryds, and Y. Z. Chen, Nano Lett. **17**, 6878 (2017).

[5] A. Brinkman, M. Huijben, M. Van Zalk, J. Huijben, U. Zeitler, J. C. Maan, W. G. Van Der Wiel, G. Rijnders, D. H. A. Blank, and H. Hilgenkamp, Nat. Mater. **6**, 493 (2007).

[6] B. Kalisky, J. A. Bert, B. B. Klopfer, C. Bell, H. K. Sato, M. Hosoda, Y. Hikita, H. Y. Hwang, and K. A. Moler, Nat. Commun. **3**, 922 (2012).

[7] D. V. Christensen, Y. Frenkel, Y. Z. Chen, Y. W. Xie, Z. Y. Chen, Y. Hikita, A. Smith, L. Klein, H. Y. Hwang, N. Pryds, and B. Kalisky, Nat. Phys. **15**, 269 (2019).

[8] A. D. Caviglia, S. Gariglio, N. Reyren, D. Jaccard, T. Schneider, M. Gabay, S. Thiel, G. Hammerl, J. Mannhart, and J. M. Triscone, Nature (London) **456**, 624 (2008).

[9] A. Joshua, S. Pecker, J. Ruhman, E. Altman, and S. Ilani, Nat. Commun. **3**, 1129 (2012).

[10] G. Herranz, G. Singh, N. Bergeal, A. Jouan, J. Lesueur, J. Gázquez, M. Varela, M. Scigaj, N. Dix, F. Sánchez, and J. Fontcuberta, Nat. Commun. **6**, 6028 (2015).

[11] F. Trier, G. E. D. K. Prawiroatmodjo, Z. Zhong, D. V. Christensen, M. von Soosten, A. Bhowmik, J. M. G. Lastra, Y. Z. Chen, T. S. Jespersen, and N. Pryds, Phys. Rev. Lett. **117**, 096804 (2016).

[12] C. H. Ahn, J. M. Triscone, and J. Mannhart, Nature (London) **424**, 1015 (2003).

[13] D. V. Christensen, F. Trier, W. Niu, Y. L. Gan, Y. Zhang, T. S. Jespersen, Y. Z. Chen, and N. Pryds, Adv. Mater. Interfaces **6**, 1900772 (2019).

[14] F. Trier, D. V. Christensen, and N. Pryds, J. Phys. D: Appl. Phys. **51**, 293002 (2018).

[15] S. Thiel, G. Hammerl, A. Schmehl, C. W. Schneider, and J. Mannhart, Science **313**, 1942 (2006).

[16] Y. C. Liao, T. Kopp, C. Richter, A. Rosch, and J. Mannhart, Phys. Rev. B **83**, 075402 (2011).

[17] D. Stornaiuolo, C. Cantoni, G. M. De Luca, R. Di Capua, E. Di Gennaro, G. Ghiringhelli, B. Jouault, D. Marrè, D. Massarotti, F. M. Granozio, I. Pallecchi, C. Piamonteze, S. Rusponi, F. Tafuri, and M. Salluzzo, Nat. Mater. **15**, 278 (2016).

[18] J. Mannhart and D. G. Schlom, Science **327**, 1607 (2010).

[19] J. Varignon, L. Vila, A. Barthélémy, and M. Bibes, Nat. Phys. **14**, 322 (2018).

[20] Y. Z. Chen, F. Trier, T. Wijnands, R. J. Green, N. Gauquelin, R. Egoavil, D. V. Christensen, G. Koster, M. Huijben, N. Bovet, S. Macke, F. He, R. Sutarto, N. H. Andersen, J. A. Sulpizio, M. Honig, G. E. D. K. Prawiroatmodjo, T. S. Jespersen, S. Linderoth, S. Ilani *et al.*, Nat. Mater. **14**, 801 (2015).

[21] T. Fix, F. Schoofs, J. L. MacManus-Driscoll, and M. G. Blamire, Phys. Rev. Lett. **103**, 166802 (2009).

[22] Y. L. Gan, D. V. Christensen, Y. Zhang, H. R. Zhang, D. Krishnan, Z. C. Zhong, W. Niu, D. J. Carrad, K. Norrman, M. von Soosten, T. S. Jespersen, B. Shen, N. Gauquelin, J. Verbeeck, J. R. Sun, N. Pryds, and Y. Z. Chen, Adv. Mater. **31**, 1805970 (2019).

[23] A. E. M. Smink, J. C. de Boer, M. P. Stehno, A. Brinkman, W. G. van der Wiel, and H. Hilgenkamp, Phys. Rev. Lett. **118**, 106401 (2017).

[24] G. Bergmann, Phys. Rev. B **28**, 2914 (1983).

[25] W. Liu, S. Gariglio, A. Fête, D. Li, M. Boselli, D. Stornaiuolo, and J. M. Triscone, APL Mater. **3**, 62805 (2015).

[26] S. Maekawa and H. Fukuyama, J. Phys. Soc. Japan **50**, 2516 (1981).

[27] D. Stornaiuolo, B. Jouault, E. Di Gennaro, A. Sambri, M. D'Antuono, D. Massarotti, F. M. Granozio, R. Di Capua, G. M. De Luca, G. P. Pepe, F. Tafuri, and M. Salluzzo, Phys. Rev. B **98**, 075409 (2018).

[28] F. Trier, G. E. D. K. Prawiroatmodjo, M. Von Soosten, D. V. Christensen, T. S. Jespersen, Y. Z. Chen, and N. Pryds, Appl. Phys. Lett. **107**, 191604 (2015).

[29] See Supplemental Material at http://link.aps.org/supplemental/10.1103/PhysRevB.100.125134 for electric-field-induced metal-insulator transition, the two-band model for the classic magnetoresistance, theoretic model of weak antilocalization, magnetoresistance oscillations at $x = 0.3$, the anomalous Hall effect at $x = 0.25$,which includes Refs. [11,16,17,22,27,32,39,44].

[30] M. Gabay and J. M. Triscone, Nat. Phys. **9**, 610 (2013).

[31] Z. Chen, H. Yuan, Y. Xie, D. Lu, H. Inoue, Y. Hikita, C. Bell, and H. Y. Hwang, Nano Lett. **16**, 6130 (2016).
[32] F. Gunkel, C. Bell, H. Inoue, B. Kim, A. G. Swartz, T. A. Merz, Y. Hikita, S. Harashima, H. K. Sato, M. Minohara, S. Hoffmann-Eifert, R. Dittmann, and H. Y. Hwang, Phys. Rev. X **6**, 031035 (2016).
[33] C. Bell, S. Harashima, Y. Kozuka, M. Kim, B. G. Kim, Y. Hikita, and H. Y. Hwang, Phys. Rev. Lett. **103**, 226802 (2009).
[34] Y. Zhang, Y. L. Gan, D. V. Christensen, H. Zhang, A. Zakharova, C. Piamonteze, S. H. Wang, N. Pryds, B. G. Shen, J. R. Sun, and Y. Z. Chen (unpublished).
[35] M. Kohda, T. Bergsten, and J. Nitta, J. Phys. Soc. Japan **77**, 031008 (2008).
[36] T. Jungwirth and J. Wunderlich, Nat. Nanotechnol. **9**, 662 (2014).
[37] G. Bergmann, Solid State Commun. **42**, 815 (1982).
[38] S. Hikami, A. I. Larkin, and Y. Nagaoka, Prog. Theor. Phys. **63**, 707 (1980).
[39] B. L. Al'tshuler, A. G. Aronov, A. I. Larkin, and D. E. Khmel'nitskii, Zh. Eksp. Teor. Fiz. **81**, 768 (1981) [Sov. Phys. JETP **54**, 411 (1981)].
[40] S. V. Iordanskii, Y. B. Lyanda-Geller, and G. E. Pikus, Pis'ma Zh. Eksp. Teor. Fiz. **60**, 199 (1994) [JETP Lett. **60**, 206 (1994)].
[41] A. Punnoose, Appl. Phys. Lett. **88**, 252113 (2006).
[42] F. Duan and J. Guojun, *Introduction to Condensed Matter Physics* (World Scientific Publishing Co., Singapore, 2005).
[43] A. McCollam, S. Wenderich, M. K. Kruize, V. K. Guduru, H. J. A. Molegraaf, M. Huijben, G. Koster, D. H. A. Blank, G. Rijnders, A. Brinkman, H. Hilgenkamp, U. Zeitler, and J. C. Maan, APL Mater. **2**, 22102 (2014).
[44] A. D. Caviglia, S. Gariglio, C. Cancellieri, B. Sacépé, A. Fête, N. Reyren, M. Gabay, A. F. Morpurgo, and J. M. Triscone, Phys. Rev. Lett. **105**, 236802 (2010).
[45] Z. Zhong, A. Tóth, and K. Held, Phys. Rev. B **87**, 161102(R) (2013).